PAPER • OPEN ACCESS

Interfacial magnon-mediated superconductivity in twisted bilayer graphene

IOP Publishing New J. Phys. 26 (2024) 033014 https://doi.org/10.1088/1367-2630/ad2ffd

New Journal of Physics
The open access journal at the forefront of physics

Deutsche Physikalische Gesellschaft DPG
IOP Institute of Physics

Published in partnership with: Deutsche Physikalische Gesellschaft and the Institute of Physics

OPEN ACCESS

RECEIVED
16 August 2023

REVISED
26 February 2024

ACCEPTED FOR PUBLICATION
4 March 2024

PUBLISHED
14 March 2024

PAPER

Interfacial magnon-mediated superconductivity in twisted bilayer graphene

Bjørnulf Brekke*, Asle Sudbø and Arne Brataas

Center for Quantum Spintronics, Department of Physics, Norwegian University of Science and Technology, NO-7491 Trondheim, Norway

* Author to whom any correspondence should be addressed.

E-mail: bjornulf.brekke@ntnu.no

Keywords: superconductivity, magnetism, heterostructure

Supplementary material for this article is available online

Abstract

The interfacial coupling between electrons and magnons in adjacent layers can mediate an attractive electron–electron interaction and induce superconductivity. We consider magic-angle twisted bilayer graphene sandwiched between two ferromagnetic insulators to optimize this effect. As a result, magnons induce an interlayer superconducting state characterized by p-wave symmetry. We investigate two candidate ferromagnets. The van der Waals ferromagnet CrI_3 stands out because it allows compression to tune the superconducting state with an exponential sensitivity. This control adds a new dimension to the tunability of twisted bilayer graphene. Our results open a new path for exploring magnon-induced superconductivity.

Heterostructures of ferromagnets (FM) and conductors are currently attracting considerable attention in spintronics. The interfacial coupling between the localized spins and itinerant electrons gives rise to intriguing phenomena such as RKKY interactions, spin-transfer, and spin-pumping [1, 2]. Furthermore, the coupling between electrons and magnons can mediate an attractive electron–electron interaction [3–5]. This effect is analogous to the electron–phonon coupling in conventional Bardeen–Cooper–Schrieffer (BCS) superconductivity [6]. Superconductivity mediated by magnons has been studied experimentally in different materials [7–9]. Furthermore, superconductivity mediated by (antiferromagnetic) magnons might also appear in certain high-T_c superconductors [10, 11].

Superconductivity induced by interfacial coupling to magnons could exist in various material combinations. Examples are normal metals coupled to ferro- and antiferromagnets [3, 5], as well as ferromagnets and antiferromagnets coupled to the surface of topological insulators [4, 12–14]. The ferromagnetic case has also been experimentally studied [15, 16], showing a superconducting state with a critical temperature T_c significantly higher than the intrinsic superconductivity of two materials. These studies consider either surface effects or monolayer conductors.

Systems designed for interfacial magnon-mediated superconductivity require specific properties. In general, superconducting critical temperatures T_c are exponentially sensitive to interaction strength. In the present case, this is the magnon-mediated electron–electron interaction. Therefore, the electron states should be localized at the interface. Thus, the conducting layer should be as thin as possible yet stable. Furthermore, the electron density of states (DOS) should be large at the Fermi level. In fulfilling these conditions, twisted bilayer graphene (TBG) stands out as an ideal candidate [17].

Twisted bilayer graphene is a two-dimensional material. This renders the electron–magnon-induced effects in TBG more robust than in 3D normal metals, where interactions are constrained to the surface. The relative twist angle of the two graphene layers creates a long-period moiré pattern that, in turn, gives rise to flat electronic bands at certain magic angles [18–20]. At higher-order magic angles, the flat bands can be related to the quantum Hall effect [21, 22]. Flat bands at the magic angles greatly enhance the electron DOS. TBG is, therefore, a laboratory for studying the transition from weak- to strong coupling superconductivity by tuning the twist angle. Graphene can couple to conventional ferromagnets [23–25]. TBG is also an

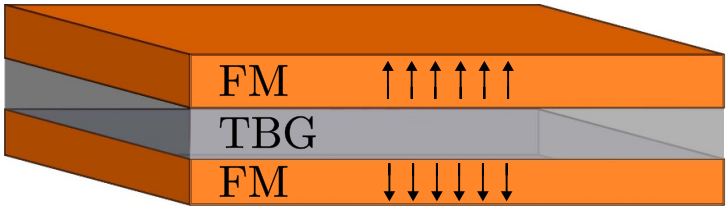

Figure 1. We consider a heterostructure consisting of twisted bilayer graphene (TBG) sandwiched between two oppositely aligned ferromagnets (FM).

interesting component of van der Waals heterostructures such as spin valves [26, 27]. Moreover, it is an intrinsic superconductor with a critical temperature of about $T_{c,\text{intrinsic}} = 1.7$ K at half filling [28]. The underlying mechanism is still under debate, and the explanations range from phonon-mediated superconductivity [29–32] to non-BCS type mechanisms [33–36].

Here, we consider another path to superconductivity in TBG via magnons in adjacent layers. Figure 1 shows twisted bilayer graphene sandwiched between two identical ferromagnets with oppositely aligned magnetization. This can be experimentally realized by sweeping a magnetic field, given that the ferromagnets have unequal coercive fields [37]. The interfacial coupling to magnons gives rise to an effective electron–electron interaction. In combination, TBG's valley degree of freedom causes a multicomponent superconductor. We find that two of the interlayer coupling channels are suitable for Cooper pair formation. Using a BCS model, we find a p-wave superconducting state with a critical temperature of the same order of magnitude as that of the intrinsic mechanism.

To describe the heterostructure, we use a Hamiltonian $H = H_{\text{TBG}} + H_{\text{FM}} + H_{\text{int}}$, where the first term describes the electrons in the twisted bilayer of graphene sheets, and the second term describes the magnons in the top and bottom layer ferromagnets. The last term describes the interfacial coupling between the ferromagnets and the graphene layers.

We consider a continuum model for the ferromagnets given by

$$H_{\text{FM}} = \int \mathrm{d}^2\boldsymbol{r}\left[J(\nabla \boldsymbol{m})^2 - K_z m_z^2)\right], \tag{1}$$

where $\mathbf{m}$ is the magnetization, $J > 0$ is the exchange coupling, and the easy-axis anisotropy is parametrized by $K_z > 0$. A Holstein–Primakoff transformation to second order in magnon operators and a subsequent Fourier transform yields the magnon Hamiltonian

$$H_{\text{FM}} = \sum_{\boldsymbol{q}} \omega_{\boldsymbol{q}} \left(a_{\boldsymbol{q}}^\dagger a_{\boldsymbol{q}} + b_{\boldsymbol{q}}^\dagger b_{\boldsymbol{q}}\right), \tag{2}$$

where $a_{\boldsymbol{q}}^{(\dagger)}$ and $b_{\boldsymbol{q}}^{(\dagger)}$ are the magnon annihilation (creation) operators of momentum $\boldsymbol{q}$ in the top and bottom layer, respectively. The magnon dispersion is $\omega_{\boldsymbol{q}} = 2JMq^2 + 2MK_z$, where M is the ground state magnetization.

TBG consists of two graphene monolayers with a relative twist angle θ, as shown in figure 2. In the decoupled limit, the top layer has two Dirac cones K_1 and K_1'. Similarly, the bottom layer has two Dirac cones K_2 and K_2'. Because of the relative twist, the Dirac points are related by the three vectors $\boldsymbol{q}_1 = k_\theta(0,-1)^T$, $\boldsymbol{q}_2 = k_\theta\left(\sqrt{3}/2, 1/2\right)^T$ and $\boldsymbol{q}_3 = k_\theta\left(-\sqrt{3}/2, 1/2\right)^T$. Here, $k_\theta = 2k_D \sin\theta/2$ is the magnitude of $\boldsymbol{q}_j$. The coefficient k_D is the magnitude of the Dirac cone momenta in the monolayers. For decoupled layers, the electrons at crystal momentum $\boldsymbol{k}$ near K_1 or K_2 are governed by the single layer Dirac Hamiltonian $h^K(\boldsymbol{k}) = v\boldsymbol{\sigma}^* \cdot \boldsymbol{k}$, whereas the electrons near the cones K_1' and K_2' are governed by $h^{K'}(\boldsymbol{k}) = -v\boldsymbol{\sigma} \cdot \boldsymbol{k}$. Here, $\boldsymbol{\sigma}$ is the Pauli matrix vector, and v is the graphene Fermi velocity.

To model the low-energy electron bands of TBG, we use the Bistritzer–SMacDonald Hamiltonian [20]. In the following, we present the main features required to apply the model for magnon-induced superconductivity. We start with an effective spin-degenerate 4×4 Hamiltonian describing the electrons at cone K_1 and interlayer hopping in momentum space to cone K_2. It is given by

$$\mathcal{H}_{\boldsymbol{k}}^{K_1K_2} = \begin{bmatrix} h^K(\boldsymbol{k}) & T_1 & T_2 & T_3 \\ T_1^\dagger & h^K(\boldsymbol{k}_1) & 0 & 0 \\ T_2^\dagger & 0 & h^K(\boldsymbol{k}_2) & 0 \\ T_3^\dagger & 0 & 0 & h^K(\boldsymbol{k}_3) \end{bmatrix}. \tag{3}$$

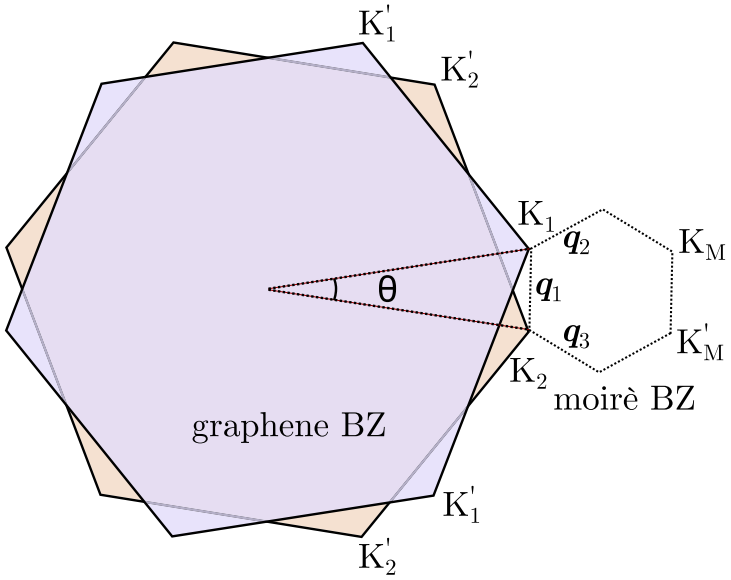

Figure 2. The Brillouin zones of two graphene layers twisted by an angle θ. These vectors constitute the moiré Brillouin zone with Dirac cones $\mathrm{K_M}$ and $\mathrm{K'_M}$.

The three other Hamiltonians describing electrons similarly at the cones (K_1', K_2, K_2') must also be considered (see supplemental material). In equation (3), each element is a 2×2 matrix in sublattice space. The Hamiltonian acts on four two-component spinors $(\psi_{K_1}(\boldsymbol{k}), \psi_{K_2}(\boldsymbol{k}_1), \psi_{K_2}(\boldsymbol{k}_2), \psi_{K_2}(\boldsymbol{k}_3))^T$. Here, the first spinor component describes electrons near K_1, whereas the other three components describe the electrons near K_2. The crystal momentum $\boldsymbol{k}_j \equiv \boldsymbol{k} - \boldsymbol{q}_j$, where $\boldsymbol{k}$ is measured relative to the top layer's Dirac cone $\mathrm{K_1}$. The Hamiltonian at K_1 couples to the Dirac cone K_2 through three hopping processes. The interlayer hopping is captured by the hopping matrices $T_1 = w(\sigma_0 + \sigma_x)$, $T_2 = w\left(\sigma_0 - 1/2\sigma_x - \sqrt{3}/2\sigma_y\right)$ and $T_3 = w\left(\sigma_0 - 1/2\sigma_x - \sqrt{3}/2\sigma_y\right)$. The hopping strength $w \approx 113$ meV [38].

The Hamiltonian in equation (3) exhibits low-energy eigenstates

$$\Psi^{K_1K_2} = \left(1, \quad -h_1^{-1}T_1^\dagger, \quad -h_2^{-1}T_2^\dagger, \quad -h_3^{-1}T_3^\dagger\right)^T, \tag{4}$$

where we used the shorthand notation $h_j = h^K(-q_j)$. Projecting the Hamiltonian on these low-energy states, we get an effective 2×2 sublattice space Hamiltonian on the form

$$\langle \Psi^{K_1K_2} | \mathcal{H}_{\boldsymbol{k}}^{K_1K_2} | \Psi^{K_1K_2} \rangle = v^\star \boldsymbol{\sigma}^* \cdot \boldsymbol{k}. \tag{5}$$

This effective Hamiltonian has the form of a single-layer Dirac Hamiltonian with a renormalized velocity

$$\frac{v^\star}{v} = \frac{1-3\alpha^2}{1+6\alpha^2}, \tag{6}$$

where $\alpha = w/vk_\theta$. Note how $\alpha^2 = 1/3$ yields a vanishing Fermi velocity and flat bands. This value corresponds to the largest 'magic angle'.

The Hamiltonian in equation (3) models electrons at cone K_1 in the top layer and three allowed interlayer hoppings to K_2. As noted above, the related Hamiltonians for the K_1' point in the top layer and K_2 and K_2' in the bottom layer must also be considered (see supplemental material). Diagonalizing all four effective 2×2 Dirac Hamiltonians, we find the resulting Hamiltonian

$$\tilde{H}_n^{I,s}(\boldsymbol{k}) = \varepsilon_{n\boldsymbol{k}} c_{\boldsymbol{k}nIs}^\dagger c_{\boldsymbol{k}nIs}, \tag{7}$$

with a linear electron dispersion $\varepsilon_{n\boldsymbol{k}} = nv^\star|\boldsymbol{k}|$. The c-operators are creation- and annihilation operators for the upper $n=1$ and lower $n=-1$ bands. The eigenstates are superpositions of states at Dirac cones in both layers. Each state is 'based' at one of the four cones $I \in \{K_1, K_1', K_2, K_2'\}$ with a threefold contribution from the opposing layer. The relative weight of the contributions depends on the twist angle θ and interlayer hopping strength w. We index the eigenstates according to the cone at which it is based. Furthermore, s is the spin index, and the crystal momentum $\boldsymbol{k}$ is taken with respect to cone I.

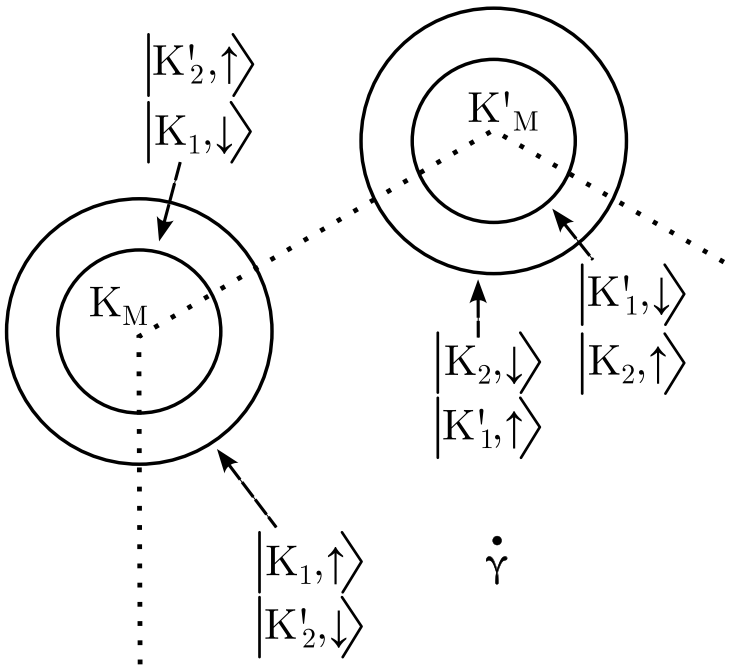

Figure 3. An intersection of the electronic bands at constant energy in the moiré Brillouin zone, with moiré cones K_M and K'_M relative to the center γ. The bands are split due to the interfacial s-d coupling giving rise to equation (9). The bands are doubly degenerate with states labeled according to the cone at which it is based and spin.

We model the interfacial coupling with a conventional *s–d* Hamiltonian

$$H_{\text{int}} = J_{s-d} \int \mathrm{d}^2 \boldsymbol{r} \boldsymbol{m}(\boldsymbol{r}) \cdot \boldsymbol{s}(\boldsymbol{r}), \tag{8}$$

where $\boldsymbol{s}$ is the spin operator of the itinerant electrons and J_{s-d} is the coupling strength.

As explained above, we take into account spin fluctuations by means of a Holstein–Primakoff transformation. We only consider the interfacial coupling between the ferromagnets and their nearest graphene layer. For instance, the first component of the electron state in equation (4) couples to the top ferromagnetic layer, whereas the three next components couple to the bottom layer. The interfacial coupling gives rise to a layer-dependent spin splitting

$$H_{\text{ss}} = \Delta_{ss} \sum_{\boldsymbol{k},I,s} ls \left(c^\dagger_{\boldsymbol{k}Is} c_{\boldsymbol{k}Is} \right), \tag{9}$$

where the spin splitting is given by

$$\Delta_{ss} = \frac{J_{s-d} M \left(1 - 6\alpha^2\right)}{1 + 6\alpha^2}. \tag{10}$$

The layer index l can be extracted directly from I. It takes the value $l = 1$ for $I \in \{K_1, K'_1\}$ and $l = -1$ for $I \in \{K_2, K'_2\}$. The spin index $s = 1$ for spin up and $s = -1$ for spin down. The spin-split electron dispersion in the moiré Brillouin zone is shown in figure 3. In the case of a monolayer conductor sandwiched between two oppositely aligned ferromagnets, the spin splitting vanishes exactly. This is not necessarily the case for a bilayer, as seen from equation (9). Each of the electron eigenstates is asymmetrically delocalized in the two layers. Hence, the net magnetic field shifts the energy of the electron states. The sign of the shift depends on spin and the layer in which the state is 'based'. At the special twist angle $\alpha^2 = 1/6$, the states are symmetrically distributed in the two layers such that the spin shift cancels.

We next consider the electron–magnon coupling

$$H_{\text{e-m}} = \sum_{\boldsymbol{q},\boldsymbol{k},I} \left[g^a_{I,\boldsymbol{k},\boldsymbol{q}} \left(c^\dagger_{\boldsymbol{k}+\boldsymbol{q}I\uparrow} c_{\boldsymbol{k}I\downarrow} \right) a_{\boldsymbol{q}} + h.c. + g^b_{I,\boldsymbol{k},-\boldsymbol{q}} \left(c^\dagger_{\boldsymbol{k}-\boldsymbol{q}I\uparrow} c_{\boldsymbol{k}I\downarrow} \right) b^\dagger_{\boldsymbol{q}} + h.c. \right]. \tag{11}$$

The coupling parameters $g^a_{I,\boldsymbol{k},\boldsymbol{q}}$ and $g^b_{I,\boldsymbol{k},-\boldsymbol{q}}$ depend on the index I, in addition to the ferromagnetic layers a and b to which it couples. Their full form is given in the supplemental material.

We derive an effective electron–electron interaction between electrons in state I and I' via a Schrieffer–Wolff transformation [39], obtaining

$$H_{\text{eff}} = \sum_{\boldsymbol{k},\boldsymbol{k}',I,I'} V_{\boldsymbol{k}\boldsymbol{k}'II'} c^{\dagger}_{\boldsymbol{k}'I\uparrow} c^{\dagger}_{-\boldsymbol{k}'I'\downarrow} c_{-\boldsymbol{k}I\downarrow} c_{\boldsymbol{k}I'\uparrow}, \tag{12}$$

where the interaction strength $V_{\boldsymbol{k}\boldsymbol{k}'II'}$ is given by

$$V_{\boldsymbol{k}\boldsymbol{k}'II'} = \frac{2\omega_{\boldsymbol{k}'+\boldsymbol{k}} \left(\sum_{j\in\{a,b\}} g^{j}_{I,-\boldsymbol{k},\boldsymbol{k}'+\boldsymbol{k}} g^{j}_{I',-\boldsymbol{k},\boldsymbol{k}'+\boldsymbol{k}} \right)}{\omega^2_{\boldsymbol{k}'+\boldsymbol{k}} - \left(\varepsilon_{\boldsymbol{k}'} - \varepsilon_{\boldsymbol{k}}\right)^2}. \tag{13}$$

The rich I, I' structure of equation (13) yields, in principle, a large number of possible pairing channels. However, not all of them are suitable for the formation of Cooper pairs. For instance, states based in the same layer with opposite spins are spin split and thus not suitable for spin-unpolarized Cooper-pairing either in the spin-singlet or spin-triplet channels. Spin-unpolarized Cooper-pairing is the only possibility when the electron–magnon coupling originates from collinear spin ground states in the magnetic insulator [40]. Hence, we focus on the coupling between electrons in different layers. This excludes half of the pairing channel candidates. Furthermore, requiring the Cooper pairs to have a zero net momentum with respect to the moiré Brillouin zone leaves two possible pairing channels. These are inter-layer intra-valley pairs denoted by

$$\{I = K_1, \bar{I} = K_2\}, \quad \{I = K_1', \bar{I} = K_2'\}. \tag{14}$$

Here, inter-layer intra-valley refers to the graphene monolayers. In the effective moiré Brillouin zone with Dirac cones K_M and K_M', this pairing is in fact an inter-valley coupling as shown in figure 3. Within these pairing channels, the interaction can be further decomposed in terms of pairing symmetry. To that end, we approximate the magnon frequency to be constant $\omega_{\boldsymbol{k}'+\boldsymbol{k}} = \omega_M$. In this approximation, the full angular dependence originates from the coupling constants g in equation (13). The effective interaction decomposes into an s-, a p-, and a d-wave component. In the low-frequency limit $(\varepsilon_{\boldsymbol{k}'} - \varepsilon_{\boldsymbol{k}})^2 \to 0$, the s- and d-wave components are repulsive. In contrast, the p-wave symmetry component is attractive and enables Cooper pair formation. Hence, we expect TBG to exhibit an interlayer magnon-mediated superconducting state with p-wave symmetry.

We now give an estimate of the critical temperature from the conventional BCS expression

$$k_B T_c \approx 1.13 \omega_M e^{-\frac{1}{\lambda}}, \tag{15}$$

where ω_M is the characteristic magnon frequency. The coupling $\lambda = V N_D'$ depends on the effective interaction V and the DOS N_D' per valley per layer per spin. The electron DOS is enhanced near the magic angle due to the flat energy bands. Carr *etal* [41] reports a total DOS $N_D \gtrapprox 100\ \text{eV}^{-1}\text{nm}^{-2}$ close to the magic angle. Since the DOS is extremely sensitive to the specific twist angle, we use the more moderate $N_D \gtrapprox 50\ \text{eV}^{-1}\text{nm}^{-2}$ in our estimates. This suggests a DOS $N_D' = 6.25\ \text{eV}^{-1}\text{nm}^{-2}$. Although the BCS theory does not predict the critical temperature, it may be used to obtain estimates of T_c. An important feature of equation (15) is the non-perturbative renormalization of the magnon energy scale, in that T_c depends exponentially on the inverse of the DOS and the interfacial s–d coupling.

The repulsive Coulomb interaction can be detrimental to the superconducting state. TBG's Coulomb interaction is largely screened at the magic angle for long wavelengths due to a large twist-angle dependent dielectric constant $\epsilon > 250$ [42]. The Coulomb coupling strength is $\mu = V_C(k_\theta) N_D \approx 1$. It slightly exceeds the attractive magnon-mediated interaction. However, for two reasons, the superconducting state is robust in the presence of this Coulomb repulsion. First, the superconducting gap function is of interlayer p-wave symmetry. Hence, the Cooper pairs circumvent the significant on-site s-wave contribution of the Coulomb interaction. However, we will not consider the decomposition of the Coulomb interaction as the approximation is already at a crude level. Second, the Coulomb interaction is frequency independent at the scale of the magnon cut-off frequencies. To account for this, we adopt the Morel–Anderson model [43] to find an effective coupling strength

$$\mu^* = \frac{\mu}{1 + \mu \ln \frac{\omega_p}{\omega_M}} \approx 0.13. \tag{16}$$

Here, we used the observed interband plasmon frequency $\omega_p \approx 200$ meV as the Coulomb interaction cut off [44]. We note that the plasmon frequency in Dirac materials is highly dependent on doping and sample

properties, perhaps best seen from the engineering of $\alpha - T_3$ materials [45–47]. However, the effective interaction strength is not particularly sensitive to the exact frequency and takes the value $\lambda^* = \lambda - \mu^*$.

Interfacial coupling between graphene and ferromagnets has been studied theoretically and experimentally for numerous materials [24, 48–53]. Hence, there are several candidates. Here, we consider two specific ferromagnets.

EuO is a ferromagnetic semiconductor with Curie temperature $T_C = 69$ K. It has an fcc unit cell with lattice constant 5.1 Å. Hence, two magnetic Eu^{2+} ions per unit cell, each with spin $S = 7/2$, are located at the interface and thus accessible for interfacial *s–d* coupling [54, 55]. EuO thin films can be deposited on graphene epitaxially [48, 49]. The induced exchange splitting is found to be $\Delta = 36$ meV [56]. At the wave number k_θ, $\omega_M = 0.15$ meV is an appropriate frequency cut-off. These parameters suggest an effective coupling strength $\lambda^* \approx 1.6$ and a superconducting critical temperature $T_c \approx 1$ K. The magnitude of λ^* suggests that we are at the limit of the validity of BCS theory and that a strong coupling approach is warranted.

CrI_3 is a van der Waals ferromagnet down to the monolayer limit [57]. The crystal has two magnetic ions per unit cell. Each magnetic ion carries a spin $S = 3/2$ [58]. CrI_3 hosts two magnonic modes accessible for electron–magnon coupling. Their respective energies at momentum $\boldsymbol{q} = 0$ are 0.3 meV and 17 meV [59]. In a graphene-CrI_3 heterostructure, CrI_3 is theoretically found to induce an exchange splitting of 20 meV [53]. Considering CrI_3 as the ferromagnet, we find a coupling constant $\lambda^* \approx 0.8$ and critical temperature $T_c \approx 1$ K.

Van der Waals ferromagnets, such as CrI_3, are particularly interesting candidates. This is because the interfacial exchange splitting increases significantly under compression. For CrI_3, a slight decrease in the interlayer gap can enhance the exchange splitting. A moderate reduction of the interlayer distance $\Delta d = -0.5$ Å leads to an exchange splitting of 80 meV. The splitting can reach values up to 150 meV [52]. The enhanced interfacial interaction renders the higher energy magnon branch of CrI_3 accessible for electron–magnon coupling. We expect this to increase the critical temperature significantly. In this way, the van der Waals spin valve exhibits a tunable compression-controlled superconducting state that connects the weak- and strong-coupling regimes. Due to the limited validity of the weak-coupling BCS model, we do not estimate the critical temperature for the compressed heterostructure.

In conclusion, we have demonstrated that interfacial magnons can induce superconductivity in twisted bilayer graphene. The magnons yield a multicomponent superconducting state due to the valley structure of TBG. We find an attractive interlayer channel suitable for Cooper pairs with *p*-wave symmetry. Moreover, we have considered two promising candidate ferromagnets, EuO and CrI_3. Both exhibit a critical temperature of the same order of magnitude as the intrinsic superconducting mechanism. The dominating mechanism must be determined experimentally. The use of van der Waals magnets is particularly interesting because the interaction strength J_{s-d} is tunable through compression. For this reason, the superconducting state is tunable both via the twist angle and external compression. Twisted bilayer graphene sandwiched between ferromagnets is, therefore, a promising platform in which to explore magnon-mediated superconductivity.

Data availability statement

No new data were created or analysed in this study.

Acknowledgments

The Research Council of Norway (RCN) supported this work through its Centres of Excellence funding scheme, Project Number 262633, 'QuSpin', as well as RCN Project Number 323766.

ORCID iD

Bjørnulf Brekke https://orcid.org/0000-0003-2265-3283

References

[1] Bruno P 1995 Theory of interlayer magnetic coupling *Phys. Rev.* B **52** 411
[2] Brataas A, Kent A D and Ohno H 2012 Current-induced torques in magnetic materials *Nat. Mater.* **11** 372
[3] Rohling N, Fjærbu E L and Brataas A 2018 Superconductivity induced by interfacial coupling to magnons *Phys. Rev.* B **97** 115401
[4] Hugdal H G, Rex S, Nogueira F S and Sudbø A 2018 Magnon-induced superconductivity in a topological insulator coupled to ferromagnetic and antiferromagnetic insulators *Phys. Rev.* B **97** 195438
[5] Fjærbu E L, Rohling N and Brataas A 2019 Superconductivity at metal-antiferromagnetic insulator interfaces *Phys. Rev.* B **100** 125432
[6] Bardeen J, Cooper L N and Schrieffer J R 1957 Theory of superconductivity *Phys. Rev.* **108** 1175
[7] Saxena S *et al* 2000 Superconductivity on the border of itinerant-electron ferromagnetism in UGe_2 *Nature* **406** 587

[8] Aoki D, Huxley A, Ressouche E, Braithwaite D, Flouquet J, Brison J -P, Lhotel E and Paulsen C 2001 Coexistence of superconductivity and ferromagnetism in URhGe *Nature* **413** 613
[9] Pfleiderer C, Uhlarz M, Hayden S, Vollmer R, v. Löhneysen H, Bernhoeft N and Lonzarich G 2001 Coexistence of superconductivity and ferromagnetism in the d-band metal $ZrZn_2$ *Nature* **412** 58
[10] Si Q, Yu R and Abrahams E 2016 High-temperature superconductivity in iron pnictides and chalcogenides *Nat. Rev. Mater.* **1** 16017
[11] Lee P A, Nagaosa N and Wen X-G 2006 Doping a mott insulator: physics of high-temperature superconductivity *Rev. Mod. Phys.* **78** 17
[12] Kargarian M, Efimkin D K and Galitski V 2016 Amperean pairing at the surface of topological insulators *Phys. Rev. Lett.* **117** 076806
[13] Erlandsen E, Brataas A and Sudbø A 2020 Magnon-mediated superconductivity on the surface of a topological insulator *Phys. Rev.* B **101** 094503
[14] Thingstad E, Erlandsen E and Sudbø A 2021 Eliashberg study of superconductivity induced by interfacial coupling to antiferromagnets *Phys. Rev.* B **104** 014508
[15] Gong X-X, Zhou H-X, Xu P-C, Yue D, Zhu K, Jin X-F, Tian H, Zhao G-J and Chen T-Y 2015 Possible p-wave superconductivity in epitaxial Bi/Ni bilayers *Chinese Phys. Lett.* **32** 067402
[16] Gong X, Kargarian M, Stern A, Yue D, Zhou H, Jin X, Galitski V M, Yakovenko V M and Xia J 2017 Time-reversal symmetry-breaking superconductivity in epitaxial bismuth/nickel bilayers *Sci. Adv.* **3** e1602579
[17] Andrei E Y and MacDonald A H 2020 Graphene bilayers with a twist *Nat. Mater.* **19** 1265
[18] Li G, Luican A, Lopes dos Santos J, Castro Neto A, Reina A, Kong J and Andrei E 2010 Observation of Van Hove singularities in twisted graphene layers *Nat. Phys.* **6** 109
[19] Suárez Morell E, Correa J D, Vargas P, Pacheco M and Barticevic Z 2010 Flat bands in slightly twisted bilayer graphene: tight-binding calculations *Phys. Rev.* B **82** 121407
[20] Bistritzer R and MacDonald A H 2011 Moiré bands in twisted double-layer graphene *Proc. Natl Acad. Sci.* **108** 12233
[21] Navarro-Labastida L A and Naumis G G 2023 3/2 magic angle quantization rule of flat bands in twisted bilayer graphene and its relationship to the quantum Hall effect *Phys. Rev.* B **107** 155428
[22] Navarro-Labastida L A and Naumis G G 2024 Self-duality properties, localization centers and magnetic energy of the electronic wave functions at small magic angles in twisted bilayer graphene *Phys. Rev.* B **109** 035402
[23] Haugen H, Huertas-Hernando D and Brataas A 2008 Spin transport in proximity-induced ferromagnetic graphene *Phys. Rev.* B **77** 115406
[24] Wei P, Lee S, Lemaitre F, Pinel L, Cutaia D, Cha W, Katmis F, Zhu Y, Heiman D and Hone J 2016 Strong interfacial exchange field in the graphene/EuS heterostructure *Nat. Mater.* **15** 711
[25] Wu Y-F *et al* 2017 Magnetic proximity effect in graphene coupled to a $BiFeO_3$ nanoplate *Phys. Rev.* B **95** 195426
[26] Geim A K and Grigorieva I V 2013 Van der Waals heterostructures *Nature* **499** 419
[27] Cardoso C, Soriano D, García-Martínez N A and Fernández-Rossier J 2018 *Van der waals spin valves Phys. Rev. Lett.* **121** 067701
[28] Cao Y, Fatemi V, Fang S, Watanabe K, Taniguchi T, Kaxiras E and Jarillo-Herrero P 2018 Unconventional superconductivity in magic-angle graphene superlattices *Nature* **556** 43
[29] Lian B, Wang Z and Bernevig B A 2019 Twisted bilayer graphene: a phonon-driven superconductor *Phys. Rev. Lett.* **122** 257002
[30] Wu F, MacDonald A H and Martin I 2018 Theory of phonon-mediated superconductivity in twisted bilayer graphene *Phys. Rev. Lett.* **121** 257001
[31] Peltonen T J, Ojajärvi R and Heikkilä T T 2018 Mean-field theory for superconductivity in twisted bilayer graphene *Phys. Rev.* B **98** 220504
[32] Choi Y W and Choi H J 2018 Strong electron-phonon coupling, electron-hole asymmetry and nonadiabaticity in magic-angle twisted bilayer graphene *Phys. Rev.* B **98** 241412
[33] Isobe H, Yuan N F Q and Fu L 2018 Unconventional superconductivity and density waves in twisted bilayer graphene *Phys. Rev.* X **8** 041041
[34] Roy B and Juričić V 2019 Unconventional superconductivity in nearly flat bands in twisted bilayer graphene *Phys. Rev.* B **99** 121407
[35] Yankowitz M, Chen S, Polshyn H, Zhang Y, Watanabe K, Taniguchi T, Graf D, Young A F and Dean C R 2019 Tuning superconductivity in twisted bilayer graphene *Science* **363** 1059
[36] Lu X *et al* 2019 Superconductors, orbital magnets and correlated states in magic-angle bilayer graphene *Nature* **574** 653
[37] Dieny B, Speriosu V S, Parkin S S P, Gurney B A, Wilhoit D R and Mauri D 1991 Giant magnetoresistive in soft ferromagnetic multilayers *Phys. Rev.* B **43** 1297
[38] Jung J, Raoux A, Qiao Z and MacDonald A H 2014 Ab initio theory of moiré superlattice bands in layered two-dimensional materials *Phys. Rev.* B **89** 205414
[39] Schrieffer J R and Wolff P A 1966 Relation between the Anderson and Kondo Hamiltonians *Phys. Rev.* **149** 491
[40] Mæland K and Sudbø A 2023 Topological Superconductivity Mediated by Skyrmionic Magnons *Phys. Rev. Lett.* **130** 156002
[41] Carr S, Fang S, Zhu Z and Kaxiras E 2019 Exact continuum model for low-energy electronic states of twisted bilayer graphene *Phys. Rev. Res.* **1** 013001
[42] Goodwin Z A H, Corsetti F, Mostofi A A and Lischner J 2019 Attractive electron-electron interactions from internal screening in magic-angle twisted bilayer graphene *Phys. Rev.* B **100** 235424
[43] Morel P and Anderson P W 1962 Calculation of the superconducting state parameters with retarded electron-phonon interaction *Phys. Rev.* **125** 1263
[44] Hesp N C, Torre I, Rodan-Legrain D, Novelli P, Cao Y, Carr S, Fang S, Stepanov P, Barcons-Ruiz D and Herzig Sheinfux H 2021 Observation of interband collective excitations in twisted bilayer graphene *Nat. Phys.* **17** 1162
[45] Malcolm J D and Nicol E J 2016 Frequency-dependent polarizability, plasmons and screening in the two-dimensional pseudospin-1 dice lattice *Phys. Rev.* B **93** 165433
[46] Iurov A, Zhemchuzhna L, Gumbs G, Huang D, Fekete P, Anwar F, Dahal D and Weekes N 2021 Tailoring plasmon excitations in $\alpha - \mathcal{T}_3$ armchair nanoribbons *Sci. Rep.* **11** 20577
[47] Iurov A, Zhemchuzhna L, Gumbs G, Huang D, Dahal Danhong and Abranyos Y 2022 Finite-temperature plasmons, damping and collective behavior in the $\alpha - \mathscr{T}_3$ model *Phys. Rev.* B **105** 245414
[48] Swartz A G, Odenthal P M, Hao Y, Ruoff R S and Kawakami R K 2012 Integration of the ferromagnetic insulator EuO onto graphene *ACS Nano* **6** 10063
[49] Averyanov D V, Sokolov I S, Tokmachev A M, Parfenov O E, Karateev I A, Taldenkov A N and Storchak V G 2018 High-temperature magnetism in graphene induced by proximity to EuO *ACS Appl. Mater. Interfaces* **10** 20767

[50] Wang Z, Tang C, Sachs R, Barlas Y and Shi J 2015 Proximity-induced ferromagnetism in graphene revealed by the anomalous Hall effect *Phys. Rev. Lett.* **114** 016603
[51] Farooq M U and Hong J 2019 Switchable valley splitting by external electric field effect in graphene/CrI_3 heterostructures *npj 2D Mater. Appl.* **3** 1
[52] Zhang J, Zhao B, Zhou T, Xue Y, Ma C and Yang Z 2018 Strong magnetization and Chern insulators in compressed graphene/CrI_3 van der Waals heterostructures *Phys. Rev.* B **97** 085401
[53] Holmes A M, Pakniyat S, Gangaraj S A H, Monticone F, Weinert M and Hanson G W 2020 Exchange splitting and exchange-induced nonreciprocal photonic behavior of graphene in CrI_3-graphene van der Waals heterostructures *Phys. Rev.* B **102** 075435
[54] Mauger A and Godart C 1986 The magnetic, optical and transport properties of representatives of a class of magnetic semiconductors: the europium chalcogenides *Phys. Rep.* **141** 51
[55] Dietrich O W, Henderson A J and Meyer H 1975 Spin-wave analysis of specific heat and magnetization in EuO and EuS *Phys. Rev.* B **12** 2844
[56] Yang H X, Hallal A, Terrade D, Waintal X, Roche S and Chshiev M 2013 Proximity effects induced in graphene by magnetic insulators: first-principles calculations on spin filtering and exchange-splitting gaps *Phys. Rev. Lett.* **110** 046603
[57] Huang B, Clark G, Navarro-Moratalla E, Klein D R, Cheng R, Seyler K L, Zhong D, Schmidgall E, McGuire M A and Cobden D H 2017 Layer-dependent ferromagnetism in a van der Waals crystal down to the monolayer limit *Nature* **546** 270
[58] McGuire M A, Dixit H, Cooper V R and Sales B C 2015 Coupling of crystal structure and magnetism in the layered, ferromagnetic insulator CrI_3 *Chem. Mater.* **27** 612
[59] Cenker J, Huang B, Suri N, Thijssen P, Miller A, Song T, Taniguchi T, Watanabe K, McGuire M A and Xiao D *et al* 2021 Direct observation of two-dimensional magnons in atomically thin CrI_3 *Nat. Phys.* **17** 20